Retrieval of Sea Surface Currents and Directional Wave Spectra by 24 GHz FMCW MIMO Radar

Giovanni Ludeno, Ilaria Catapano, Francesco Soldovieri, *Senior Member, IEEE*, and Gianluca Gennarelli

***Abstract*— This article investigates the capabilities of 24 GHz frequency-modulated continuous-wave (FMCW) multiple-input–multiple-output (MIMO) radar technology to retrieve sea surface currents and directional wave spectra. A procedure based on the dispersion relation, which was previously applied to process X-band marine radar data, is here exploited. The estimation performance of the radar sensor is first assessed by numerical tests in the case of synthetic sea wave fields with known characteristics in terms of wave direction and surface currents. Finally, the estimation procedure is assessed on real data collected at San Vincenzo quay in the port area of Naples, Italy. The achieved results are encouraging and highlight that 24 GHz FMCW MIMO radar is a viable technology for sea wave monitoring.**

***Index Terms*— Directional spectrum, frequency-modulated continuous wave (FMCW), multiple-input–multiple-output (MIMO) radar, sea wave monitoring, surface currents.**

I. Introduction

REMOTE sensing technologies, such as radars [1], altimeters [2], and video-monitoring systems [3], [4], have attracted considerable attention for sea state monitoring in recent years. Indeed, they permit a noninvasive and remote observation of the sea surface in severe weather and sea wave conditions, thus providing a valid alternative to classical in situ sensors (e.g., wave rider buoy and acoustic Doppler current profiler) [5].

Among these technologies, radar systems have proven effective for measuring wave spectra and retrieving sea state information. Indeed, they are widely used also due to their flexibility to be mounted on different observation platforms ranging from spaceborne to land-based ones [6]. Radar systems mounted on satellites, which usually operate at L-, C-, X-, Ka-, and Ku-bands, allow observing wide areas and are employed to retrieve the direction, wavelength, wave height, and sea surface currents at a regional scale [7], [8]. However, the operation of radars on satellites is affected by several factors, such as the long revisit time determined by orbit characteristics and latitude, and the coarse spatial resolution [7]. More recently, the exploitation of airborne X-band radars has also been addressed [9]. These systems are more flexible than satellite-based ones, but their high mission costs do not allow continuous sea state monitoring over time.

Ground-based radar systems, such as high-frequency radar (HFR), marine radar (MR), and short-range K-band (SRK-band) radar, allow overcoming the limitations of the aforementioned systems. In particular, HFR operates in the 3–30 MHz frequency band (i.e., wavelengths of 10–100 m) and can provide a relatively wide range coverage (up to 200 km) with a high temporal and spatial resolution. The range resolution of HFR typically varies from a few hundred meters to 12 km, while azimuth resolution is both platform and algorithm-dependent, with typical values between 5° and 18° [10]. HFR plays an essential role in monitoring surface currents and wave spectra and has become a standard and cost-effective component for global ocean wave observation [11].

MR operates at S-band (2–4 GHz) or X-band (8–12 GHz), with wavelengths approximately equal to 12 and 3 cm in air, respectively. MR allows observations in a range of a few kilometers from the platform and provides an improved spatial resolution (e.g., meters) than HFR. As shown in [12], X-band radar is preferred to S-band one since its smaller wavelength guarantees a higher resolution. Nevertheless, S-band radar is a valid alternative to X-band radar in the presence of heavy rainfall [13], where wave attenuation and scattering phenomena can impair the quality of data. MRs can be classified into two groups: noncoherent and coherent radars. The first one considers only the amplitude of the radar data, while the second one considers also the phase information. The noncoherent radar is commonly used to retrieve various sea state parameters such as the wavelength, period, and direction of the dominant waves from 2-D wave spectra [14], significant wave height [15], [16], maps of the sea surface elevation [17], surface currents, and bathymetry [18], [19]. In addition, these radars are useful to retrieve the sea state information from a moving ship [20], [21]. However, a drawback of noncoherent MRs is the need for a modulation transfer function (MTF) to calibrate the radar spectrum and get a reliable estimation of the sea state parameters (significant wave height, period, and wavelength) [17], [22], [23]. Differently from noncoherent MRs, coherent systems consider also the phase of signal or the target radial velocity (Doppler shift), from which it is possible to retrieve the significant wave height and 2-D directional spectra, and quantify some physical characteristics of the sea wave [24], [25]. Moreover, coherent MRs do not require the calibration of the radar spectrum needed by noncoherent systems [24].

Manuscript received 4 August 2022; revised 25 October 2022 and 2 December 2022; accepted 29 December 2022. Date of publication 12 January 2023; date of current version 24 January 2023. *(Corresponding author: Gianluca Gennarelli.)*

The authors are with the Institute for Electromagnetic Sensing of the Environment, National Research Council of Italy, 80124 Naples, Italy (e-mail: gennarelli.g@irea.cnr.it).

Digital Object Identifier 10.1109/TGRS.2023.3236359

More recently, the use of SRK-band radars has been proposed for sea state monitoring [26], [27], [28]. These systems operate in the 18–27 GHz frequency band, i.e., wavelengths in the range of 0.016–0.01 m. Specifically, a strategy was proposed in [27] to retrieve ocean wave parameters using an SRK-band narrow beam continuous-wave radar. The estimation methodology was validated through numerical simulations and experiments carried out in a tank with regular waves generated under ideal conditions. Later in [28], the same radar was tested to measure the spectra of wind waves at sea. Note that the aforementioned systems are used to monitor the sea state by pointing the radar in the direction of the incoming wave and local wind. Therefore, they provide only spatial information about the sea state along one dimension.

SRK-band radars are complementary to the aforementioned land-based systems for sea state monitoring. They are usually characterized by a small range coverage (e.g., up to a few hundred meters), which is useful for analyzing sea waves very close to the coast and in semiclosed areas (e.g., bay and harbor). Moreover, SRK-band radars have a high temporal and spatial resolution, which makes them sensitive to wind-generated capillary waves. Further advantages of SRK-band radars are their small size, low weight, and reduced electromagnetic emissions. These peculiar features enable their installation on platforms with a limited payload such as autonomous surface vehicles (ASVs) to perform wave height measurements [26] or target detection [29] and tracking [30] for enhancing navigational safety.

In this article, we investigate the application of a 24 GHz frequency-modulated continuous-wave (FMCW) multiple-input–multiple-output (MIMO) radar for sea wave monitoring. The radar was originally developed for automotive applications [31] and its target detection and tracking capabilities in the marine environment have been recently demonstrated [30]. The radar signal processing pipeline here proposed consists of two main steps: radar imaging and sea currents and directional wave spectrum estimation. In the first step, spatial-domain beamforming [32] is implemented to obtain a focused image of the scene from the baseband raw radar signals. In the second stage, the temporal sequence of focused radar images is processed to retrieve information about the sea waves in terms of surface current fields and directional spectrum. To achieve this goal, we exploit the dispersion relation characterizing the sea wave spectrum as done for X-band MR data [19], [33], [34]. The estimation capabilities of the FMCW MIMO radar are evaluated first with synthetic radar images and after by processing real data.

As regards the numerical simulations, a synthetic sea wave simulator is developed by applying the Fourier domain approach [35], [36] and considering the Pierson–Moskowitz model [37] for the sea wave spectrum. Then, a 3-D simulator of FMCW MIMO radar data is developed and implemented by considering the backscattering from the capillary waves and modulation phenomena (shadowing and tilt modulation) affecting the radar echoes, which depends on the generated sea model and radar antenna geometry.

Experimental data collected at San Vincenzo quay in the port area of Naples, Italy, are processed to test the performance of the radar system.

It must be pointed out that the originality of this work regards the possibility to retrieve 2-D spatial information of sea waves by SRK-band FMCW MIMO radar data. This claim is supported by a numerical analysis involving the generation of a temporal sequence of radar data in known sea conditions. Moreover, a preliminary field test is carried out to verify the considered SRK-band radar's potential. Note that, unlike conventional MRs, the peculiar features of SRK-band radar (i.e., low weight and small size) allow planning a measurement campaign in a very fast and inexpensive way.

This article is organized as follows. Section II briefly describes the MIMO radar platform and the related signal model. The models and methods to generate synthetic sea wave and radar data are presented in Section III. The radar data processing chain is described in Section IV. Numerical and experimental results are shown in Sections V and VI, respectively. Concluding remarks follow in Section VII.

II. FMCW MIMO Radar Sensor

This section describes the FMCW MIMO radar platform for sea wave monitoring and the related signal model for the case of a point target. Such a model provides the basis for simulating the radar data in the presence of a sea wave field (WF) (see Section III-B).

A. System Description

The radar platform RadarBook2 [31] manufactured by Inras Gmbh for automotive purposes is here considered. The platform is based on an FMCW MIMO architecture equipped with two transmitting (Tx) and eight receiving (Rx) antennas operating in the 24–24.25 GHz frequency range (K-band). The antennas are linearly polarized patch arrays (eight radiating elements) with a narrow beam in the vertical plane ($\pm 6.4°$) and a broad beam in the horizontal plane ($\pm 75°$). The radar is compact and lightweight with an approximate size of 13.5 $\times$ 4 $\times$ 11 cm and about 0.5-kg weight. The radar provides a short-range coverage, e.g., 75 m for a target radar cross section (RCS) of 0 dBm^2 and single pulse processing. Fig. 1 shows the RF front end of the RadarBook2 platform.

As regards the spatial resolution, the system is characterized by a range resolution $\Delta r = 0.6$ m, while the angular resolution depends on the target direction θ from the boresight (y-axis or $\theta = 0$). Specifically, the finest angular resolution (about 7.6°) is achieved when the target is illuminated at the boresight. Moreover, the resolution degrades progressively as the target moves away from boresight reaching a value around 30° at the edges of the nominal azimuth field of view (FoV) ($\pm 75°$).

Table I summarizes the main electrical radar parameters. The system is also equipped with a baseband board (not shown in Fig. 1), which is responsible for the radar configuration, data acquisition, and data transfer to a PC. More details about the RadarBook2 platform can be found in [30] and [31].

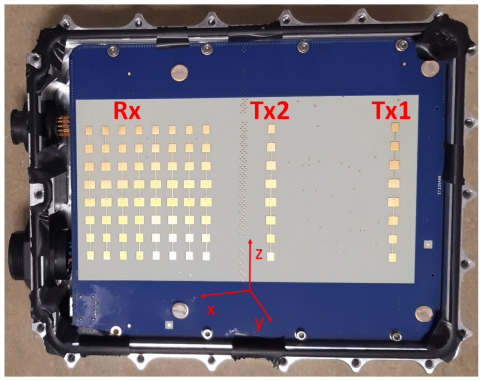

Fig. 1. Photograph of RadarBook2 RF front end.

TABLE I
RADAR PARAMETERS

Parameter	Value	Unit
Center frequency	24.125	GHz
Bandwidth	250	MHz
Azimuth field of view	± 75	[°]
Elevation field of view	± 6.4	[°]
Antenna gain	13.5	dB
Range resolution	0.6	m
Min angular resolution	7.6 @ 0°	[deg]
Max angular resolution	30 @± 75°	[deg]
Power absorption	14	W
Supply DC voltage	12-36	V

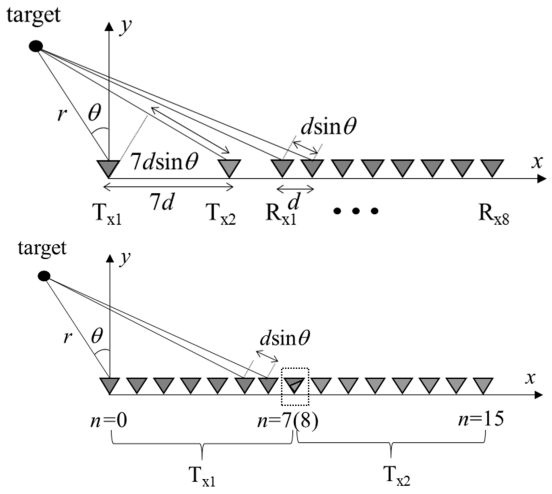

Fig. 2. (Top) Actual MIMO antenna configuration. (Bottom) Equivalent virtual array with overlap between eighth and ninth element. A point target is located at (r, θ).

B. Signal Model

The top panel of Fig. 2 shows the spatial arrangement of the 2×8 MIMO radar antennas, which are aligned along the x-axis of the reference system. The spacing between the Tx antennas (Tx_1 and Tx_2) is equal to $7\lambda_c/2$ (λ_c is the free-space wavelength at the center frequency), while the spacing between the Rx antennas is $d = \lambda_c/2$. Based on the spacing between Tx and Rx antennas, the 2×8 MIMO array is equivalent to a monostatic virtual array of 16 antennas (channels), with an overlap between the eighth and ninth elements [30]. This concept is graphically represented in the bottom panel of Fig. 2. The number of channels considered for sea wave monitoring is defined by the set of indices $\{n = 0, \ldots, 15, n \neq 8\}$.

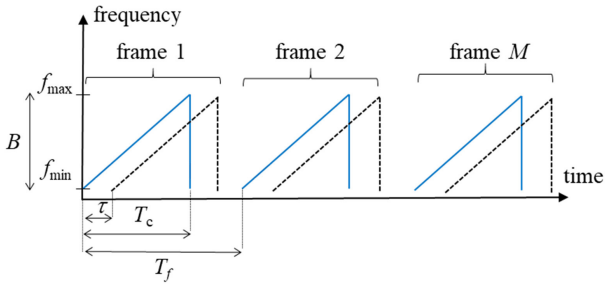

Fig. 3. Time–frequency representation of FMCW radar waveforms for a single radar channel over successive M scans. Transmitted signal (solid line) and received signal (dashed line).

Fig. 3 shows a graphical representation of the transmitted and received FMCW waveforms for a single radar channel over successive acquisition cycles. In every cycle with duration T_f, the transmitted signal is a chirp with duration T_c and bandwidth $B = f_{\max} - f_{\min}$, i.e.,

$$x(t) = A_t \cos\left(2\pi f_{\min} t + \pi \gamma t^2\right) \tag{1}$$

where A_t is the amplitude and $\gamma = B/T_c$ is the chirp rate.

The received signal over channel n is a time-delayed version of the transmitted one, i.e.,

$$y_n(t) = A_r \cos\left(2\pi f_{\min}(t - \tau_n) + \pi \gamma (t - \tau_n)^2\right) \tag{2}$$

where

$$\tau_n = \frac{2r}{c} + \frac{nd\sin(\theta)}{c} \tag{3}$$

is the travel time to the target, A_r is the received signal amplitude, and c is the electromagnetic wave speed in air.

The received signal in (2) is demodulated by using the transmitted signal $x(t)$ as a local oscillator. Upon filtering the double frequency terms, the baseband or intermediate frequency (IF) signal can be approximated as

$$s_n(t) \approx A \cos(2\pi f_{\text{IF}} t + 2\pi f_1 \tau_n) \tag{4}$$

that is a cosinusoid at IF frequency

$$f_{\text{IF}} \approx \frac{2\gamma r}{c}. \tag{5}$$

For every frame $m = 1, \ldots, M$, the baseband signals $s_n(t)$, $n = 0, \ldots, 15, n \neq 8$, are the raw data, which are organized in the form of a matrix where time t varies along rows and radar channel n varies along columns.

III. SEA WAVE AND RADAR DATA SIMULATION

This section describes the models and the procedures for the generation of the synthetic WF and a 3-D radar signal simulator accounting for modulation effects (tilt and shadowing), which influences the amplitude of the returns from the points on the sea surface in the radar FoV.

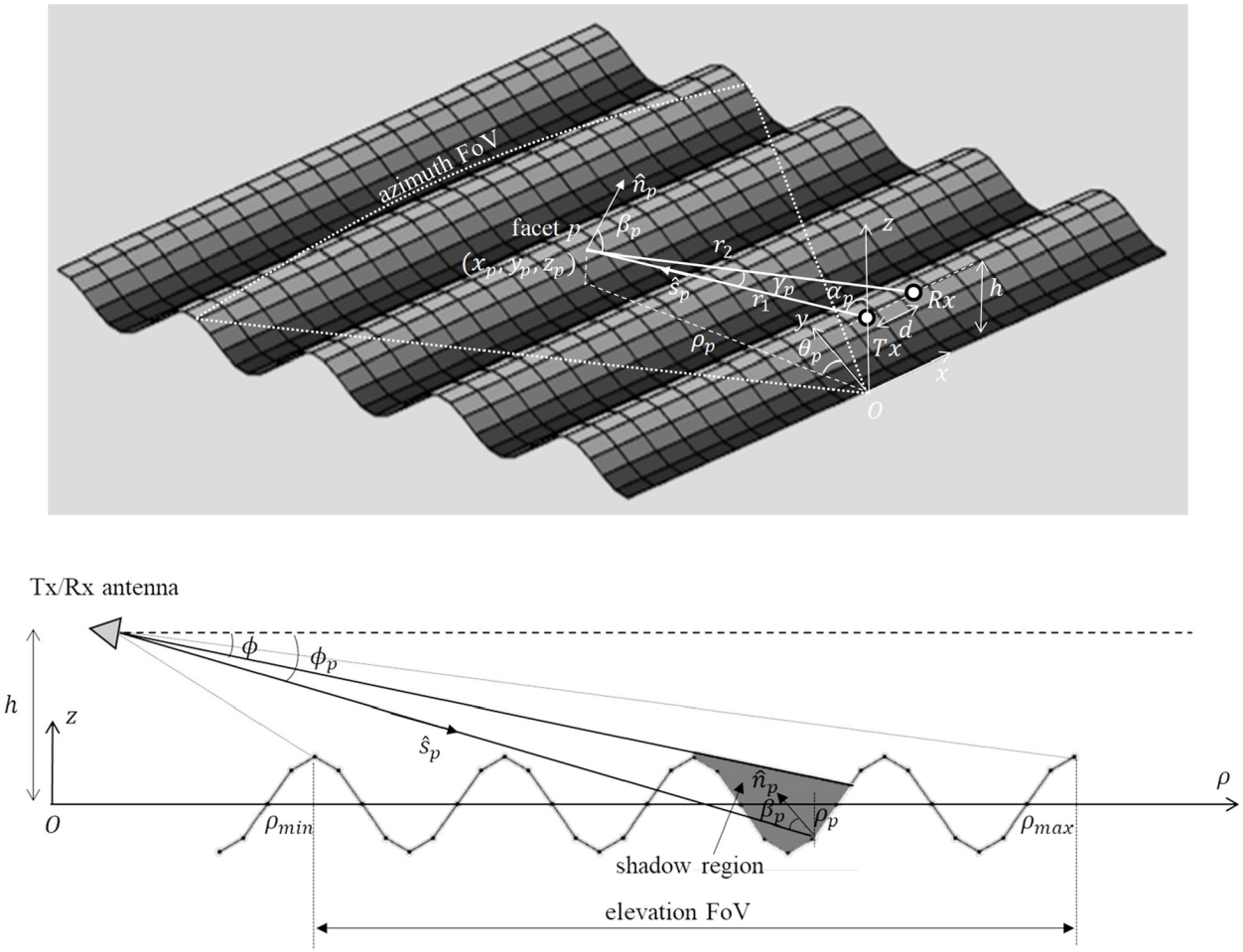

Fig. 4. (Top) 3-D geometry of the sea surface probed by a single Tx and Rx antenna pair of MIMO radar located at quota h above the MSL ($z = 0$). The dotted lines delimit the radar azimuth FoV of radar. (Bottom) Graphical representation of the shadowing effect in the vertical plane at $\theta = \theta_p$, where radar FoV is delimited by dotted lines and the shadow region is the colored area.

A. Synthetic WF Simulation

The Fourier domain approach is employed to synthesize 2-D sea waves generated by wind [35]. This approach, already adopted in [16], considers the model of deep-sea water without interaction with the coast. According to [34], the sea surface elevation $z(\bar{r}, \tilde{t})$ is modeled as a sum of sinusoids with time-dependent amplitude $\tilde{z}(\bar{k}, \tilde{t})$, i.e.,

$$z(\bar{r}, \tilde{t}) = \mathrm{Re}\left\{ \sum_{\bar{k}} \tilde{z}(\bar{k}, \tilde{t}) e^{-i\bar{k}\cdot\bar{r}} \right\} \tag{6}$$

where $\bar{k} = (k_x, k_y)$ is the wave vector with amplitude $k = |\bar{k}| = (k_x^2 + k_y^2)^{1/2}$, $\bar{r} = (x, y)$ is the position vector in the plane $z = 0$ corresponding to the mean sea level (MSL), and $\tilde{t}$ is the slow time. The set of complex Fourier domain amplitudes and their initial ($\tilde{t} = 0$) phase values for the wave elevation field is defined as

$$\tilde{z}_0(\bar{k}) = \frac{1}{\sqrt{2}} (\xi_{\mathrm{Re}} + i\xi_{\mathrm{Im}}) \sqrt{E_{\mathrm{PM}}(\bar{k})} \tag{7}$$

where ξ_{Re} and ξ_{Im} are the independent outputs from a Gaussian random number generator with zero mean and unitary standard deviation, respectively [36]. Moreover, the function defines the spectral properties of the WF and it is set in accordance with the 2-D Pierson–Moskowitz model, suitable for a fully developed wind sea [37]

$$E_{\mathrm{PM}}(\bar{k}) = \frac{\mu}{2k^4} e^{-\varepsilon \left(\frac{g}{k W_{10}^2} \right)^2} \tag{8}$$

where $\mu = 0.0081$ is the Phillips constant, $\varepsilon = 1.25$, $g = 9.81$ m/s^2 is the gravitational acceleration, and W_{10} is the wind speed at a height of 10 m above the MSL. The sea wave directional spectrum in (8) is calculated at the radar boresight (i.e., $\theta = 0°$ or $\hat{k} = \hat{k}_y$). The directional wave spectrum related to a propagation direction θ^* from the boresight is found by rotating the spectrum at boresight by the angle θ^*.

Under the linear wave theory, the sea surface waves are dispersive and their propagation mechanism is governed by the dispersion relation [38]

$$\omega(\bar{k}) = \sqrt{gk \tanh(kD)} + \bar{k} \cdot \bar{U} \tag{9}$$

where ω is the angular frequency, D is the seabed depth, and $\bar{U} = (U_x, U_y)$ is the surface current vector. Given the dispersion relation in (9), the time-dependent amplitude of the

WF elevation at time $\tilde{t}$ is expressed as

$$\tilde{z}(\overline{k},\tilde{t}) = \tilde{z}_0(\overline{k})e^{i\omega(\overline{k})\tilde{t}} + \tilde{z}_0^*(-\overline{k})e^{-i\omega(\overline{k})\tilde{t}}. \quad (10)$$

Equation (10) preserves the complex conjugate property and allows computing the sea surface elevation $z(\overline{r},\tilde{t})$ as real quantity in (6) via an inverse fast Fourier transform (IFFT) [36]. Note that, here, the sea WF is generated in deep-sea water conditions, i.e., when $\tanh(kD) \to 1$ ($kD \to \infty$).

It is stressed that (6) models only the long waves and neglects the small ripples (capillary waves) with wavelength comparable to the radar signal wavelength (e.g., about 1 cm). However, the effect of these waves on data will be accounted for by the radar simulator described in the following.

B. Radar Data Simulation

We present a simple approach to generate synthetic radar data in the time domain starting from the sea WF obtained with the procedure detailed in Section III-A. To this end, we recall that the sea surface can be seen as a superposition of long waves and capillary waves. The small ripples are responsible for the main backscattering contribution (resonant Bragg scattering), which is modulated by longer waves detected by the radar [22]. Here, we adopt a facet model to describe the scattering from the sea surface (see [39]). Therefore, the sea surface is approximated by facets, and the radar signal is evaluated as a superposition of the contributions originating from each facet in the radar FoV. It must be stressed that the sea surface presents two-scale irregularities due to long and short waves; consequently, a two-scale model [39], [40], [41] is adopted where the set of facets represents the sea surface over a large scale (long wave) and the roughness superimposed in each facet (capillary wave) models the sea surface at a small scale.

Let us refer to the 3-D geometry shown in the top panel of Fig. 4. Here, a single Tx–Rx antenna pair corresponding to a generic channel n of the virtual array in Fig. 2 is considered for the sake of simplicity since the following analysis holds also for the other antenna pairs. The Tx and Rx antennas are located at $(0, 0, h)$ and $(d, 0, h)$, respectively. The generic facet p has its center at (x_p, y_p, z_p), $\hat{n}_p$ is the normal unit vector, and $\hat{s}_p$ is the local incidence direction. Moreover, r_1 is the distance from the Tx antenna to the facet, and r_2 is the distance from the facet to the Rx antenna. Note that the distances r_1 and r_2 are much larger than d so that the angle γ_p approaches 0 and $r_2 \approx r_1 = r_p$, with r_p being the slant range from the antennas to the center of facet p. The local incidence angle β_p, i.e., the angle between the incidence direction $\hat{s}_p$ and the normal $\hat{n}_p$ to the facet p, is defined by

$$\cos\beta_p = -\hat{s}_p \cdot \hat{n}_p. \quad (11)$$

In the top panel of Fig. 4, ρ_p is the projection of the slant range r_p on the plane corresponding to the MSL ($z = 0$), which is performed according to the angle α_p. The projection forms an angle θ_p from the y-axis, corresponding to the radar boresight (see also Fig. 2).

According to the formulation of the scattering from a two-scale dielectric profile (see [39], [40], [41]) and based on (4), the radar signal reflected by the sea surface is written as the superposition of the contributions from every illuminated facet, i.e.,

$$s_n(t) \approx \sum_{p\in S} \frac{\sqrt{\sigma_{0p}A_p}}{r_p^2}\cos\left(2\pi f_{\mathrm{IF}p}t + 2\pi f_1 \tau_{np} + \Phi_p\right) \quad (12)$$

where S is the set of illuminated facets, $(1/r_p^2)$ is the two-way geometrical attenuation for a spherical wave modeling the radar signal propagation in free space, σ_{0p} is the normalized radar cross section (NRCS) of the pth facet whose area is A_p, Φ_p is the phase shift due to the backscattering from the pth facet, and

$$f_{\mathrm{IF}p} = \frac{2\gamma r_p}{c} \quad (13)$$

$$\tau_{np} = \frac{r_1 + r_2}{c}. \quad (14)$$

The NRCS σ_{0p} in (12) accounts for the backscattering from the capillary waves and is evaluated in accordance with the model reported in [42], and only the Bragg scattering contribution to the NRCS is considered [27]. Note that the NRCS modulates the returns from each illuminated facet through the local incidence angle β_p (tilt modulation) [44]. As regards the phase term Φ_p in (12), such a quantity is modeled as a uniform random variable over the interval $[-\delta_p/2, \delta_p/2]$, with δ_p being the maximum phase shift over the facet [43].

The exact expression of r_2 is considered for the evaluation of the time delays τ_{np} in (14) instead of its approximation $r_1 = r_p$. Indeed, the delays τ_{np} appear in the phase of the radar signal contributions [see (12)] and an accurate determination of the phase variation along the virtual array is necessary to achieve a satisfactory focusing along the azimuth.

The bottom panel of Fig. 4 displays the radar signal propagation in the vertical plane at a fixed azimuthal coordinate $\theta = \theta_p$ showing the tilt modulation and shadowing phenomena. As for the shadowing effect, by introducing the grazing angle ϕ_p defined by the propagation direction $\hat{s}_p$ and the horizontal direction $\hat{\rho}$, a single facet p is not illuminated if the following condition holds [44]:

$$\exists(\rho,\phi) : \phi_p > \phi, \rho < \rho_p. \quad (15)$$

The above condition means that a facet p is shadowed by a wave crest located at a closer range (i.e., $\rho < \rho_p$) from the radar.

A baseband raw data frame $s_n(t), n = 0, \ldots, 15, n \neq 8$, is evaluated at any slow time $\tilde{t} = \tilde{t}_1, \tilde{t}_2, \ldots, \tilde{t}_M$ and the data frame sequence is processed to gain information about the sea waves, as discussed in Section IV.

IV. Data Processing Strategy

A block diagram of the radar data processing pipeline is shown in Fig. 5. As can be seen, at any slow time $\tilde{t} = \tilde{t}_1, \tilde{t}_2, \ldots, \tilde{t}_M$, the signals backscattered by sea surface $s_n(t), n = 0, \ldots, 15, n \neq 8$, defined by (12), are processed according to a beamforming algorithm (see [30] for more details) based on a double fast Fourier transform (FFT), the first one along the time (range-FFT) and the second one along

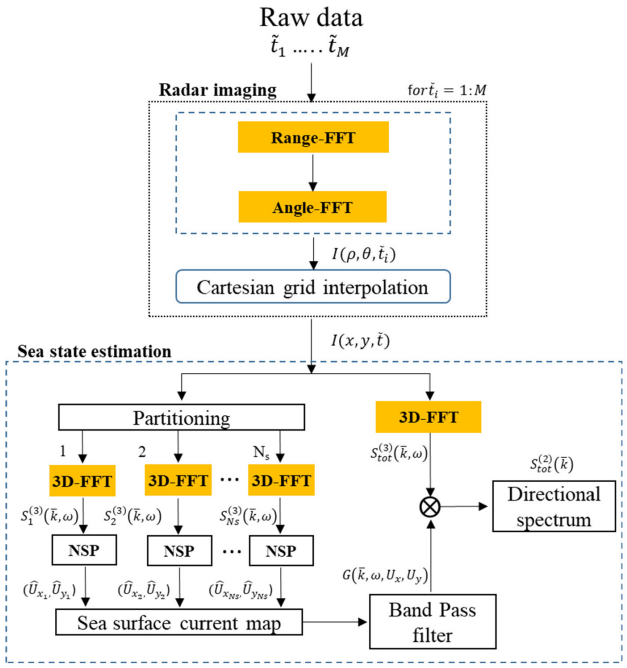

Fig. 5. Block diagram of the MIMO radar data processing chain for sea surface currents and directional wave spectrum estimation.

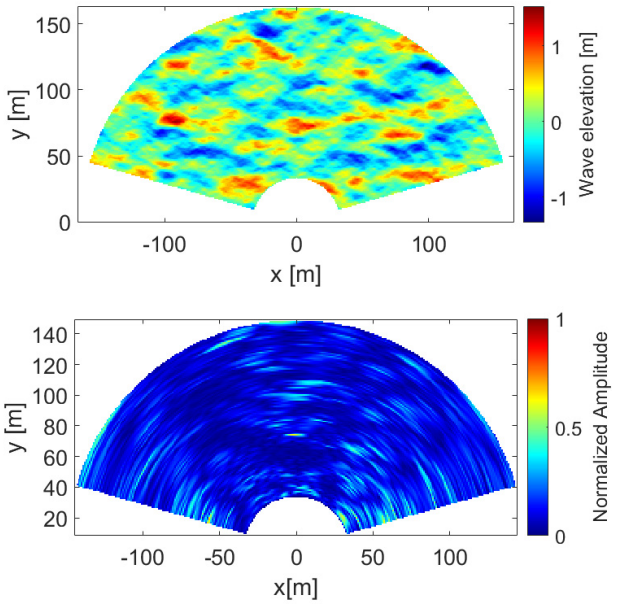

Fig. 6. Synthetic data related to WF_1 at time $\tilde{t} = 64$ s. (Top) Sea surface elevation profile. (Bottom) Radar image.

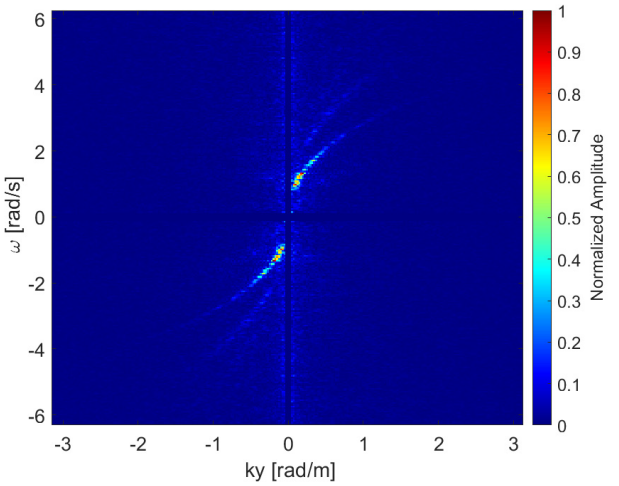

Fig. 7. Normalized amplitude of the 3-D radar data spectrum in the plane $k_x = 0$ for WF_1.

the channels (angle-FFT). In this way, after conversion from slant range r to ground range ρ on the MSL, a focused intensity image $I(\rho, \theta, \tilde{t})$ of the sea surface is achieved. This image is then converted from a polar to the Cartesian grid due to linear interpolation, thus obtaining the image $I(x, y, \tilde{t})$. Finally, the temporal sequence of intensity images $I(x, y, \tilde{t})$ is given in input to the estimation procedure as detailed in the following.

The strategy employed to reconstruct the sea surface current field from the temporal sequence of radar images $I(x, y, \tilde{t})$ follows the approach developed for processing the data acquired by incoherent X-band MRs. Such an approach has been tested and validated in previous works using both numerical and experimental data (see [19], [33], [34]).

The estimation technique involves a spatial partitioning of the radar images into N_s partially overlapping subareas and each of them is characterized by a temporal sequence of M images. Note that, in each subarea, the physical parameters of the sea are assumed to be spatially homogeneous and temporally stationary (see [17], [18], [19]).

For each subarea, the 3-D radar spectrum $\{S_j^{(3)}(\bar{k}, \omega)\}_{j=1,\ldots,N_s}$ is computed via the FFT algorithm. Hence, starting from the local radar spectra, the local components of sea surface current $(\hat{U}_{xj}, \hat{U}_{yj})$ are estimated by maximizing the normalized scalar product (NSP) [17]

$$\left(\hat{U}_{xj}, \hat{U}_{yj}\right) = \text{argmax}_{(U_x,U_y)} \frac{\left\langle \left|S_j^3\left(\bar{k},\omega\right)\right|, G\left(\bar{k},\omega,U_x,U_y\right)\right\rangle}{\sqrt{P_{S_j}}} \tag{16}$$

where $G(\bar{k}, \omega, U_x, U_y) = \delta(\omega - (gk)^{1/2} - k_x U_x - k_y U_y)$ is the characteristic function [being $\delta(\cdot)$ the Dirac-delta distribution] based on (9), $\langle \cdot, \cdot \rangle$ denotes the scalar product of the functions $|S_j^{(3)}|$ and G, and P_{S_j} is the spectrum power.

Subsequently, the sea surface currents are exploited to define a bandpass filter based on the dispersion relation [see (9)], which allows separating the sea wave contribution from the background noise in the radar spectrum $S_{\text{tot}}^{(3)}(\bar{k}, \omega)$ referred to the whole observed scenario. At this point, the 2-D directional spectrum $S_{\text{tot}}^{(2)}(\bar{k})$ is estimated as follows:

$$S_{\text{tot}}^{(2)}\left(\bar{k}\right) = \int_{\omega>0} S_{\text{tot}}^{(3)}\left(\bar{k},\omega\right) d\omega. \tag{17}$$

It is worth pointing out that the signal processing strategy in Fig. 5 provides the information about the sea surface currents and 2-D directional wave spectrum.

However, a complete characterization of the sea waves (e.g., in terms of wavelength, period, and wave height) requires

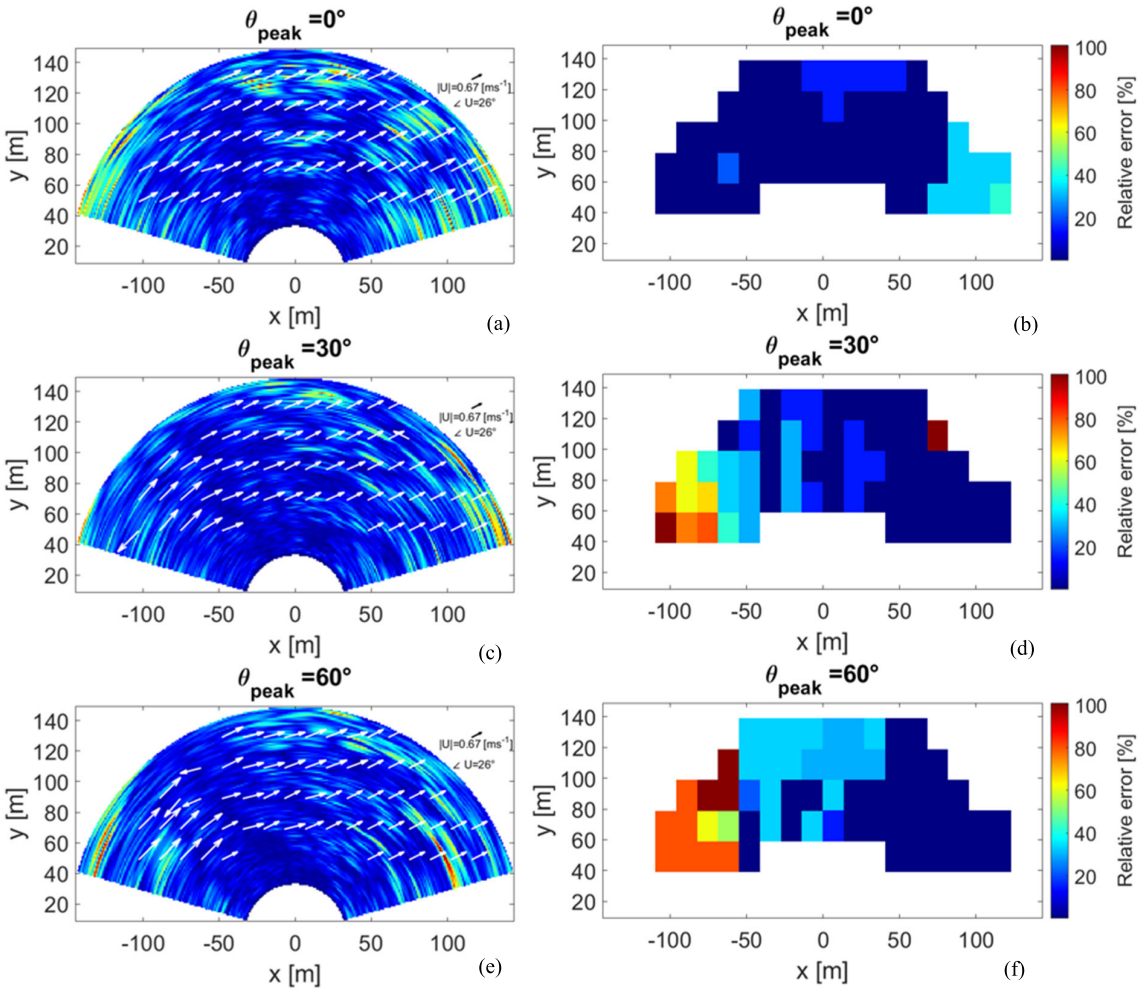

Fig. 8. (a), (c), and (e) Sea surface current maps for different WF directions superimposed on the radar image at $\tilde{t} = 5$ s. Reference values for current magnitude and direction are shown in this figure. (b), (d), and (f) RPE corresponding to the current maps.

TABLE II
MAIN CHARACTERISTICS OF SYNTHETIC WFS

	T_{peak} [s]	λ_{peak} [m]	θ_{peak} [°]	$\mathcal{W}^{10}$ [m/s]
WF_1	5	39	0	7.8
WF_2	4.5	31.5	30	7.0
WF_3	4.4	31	60	6.9

TABLE III
RADAR CONFIGURATION SETTINGS

Parameter	Description	Value	Unit
f_{start}	start frequency	24.00	[GHz]
f_{stop}	stop frequency	24.25	[GHz]
T_c	chirp duration	200	[μs]
PRI	pulse repetition interval	0.5	[s]
N_t	number of baseband samples	1024	-
f_s	baseband sampling frequency	5	[MHz]
T_w	observation time window	128	[s]
$AzFov$	azimuth FoV	150	[°]
h	radar height above the MSL	10	m
ρ_{min}	minimum range on the MSL	34	m
ρ_{max}	maximum range on the MSL	164	m

mitigating the distortions caused by the modulation phenomena related to the radar acquisition geometry. This task has been performed for X-band MRs data in previous studies [22]; however, the task is not straightforward for the considered SRK-band FMCW MIMO radar and is beyond the scope of the present study.

V. NUMERICAL RESULTS

This section provides a numerical assessment of the data processing strategy presented in Section IV. The simulations have been carried out by using ad hoc codes developed under MATLAB 2019 environment.

Three synthetic sea WFs characterized by a moderate state and deep-sea water conditions are generated in accordance with the Douglas scale [45]. Specifically, different peak values are considered for the period T_{peak}, wavelength

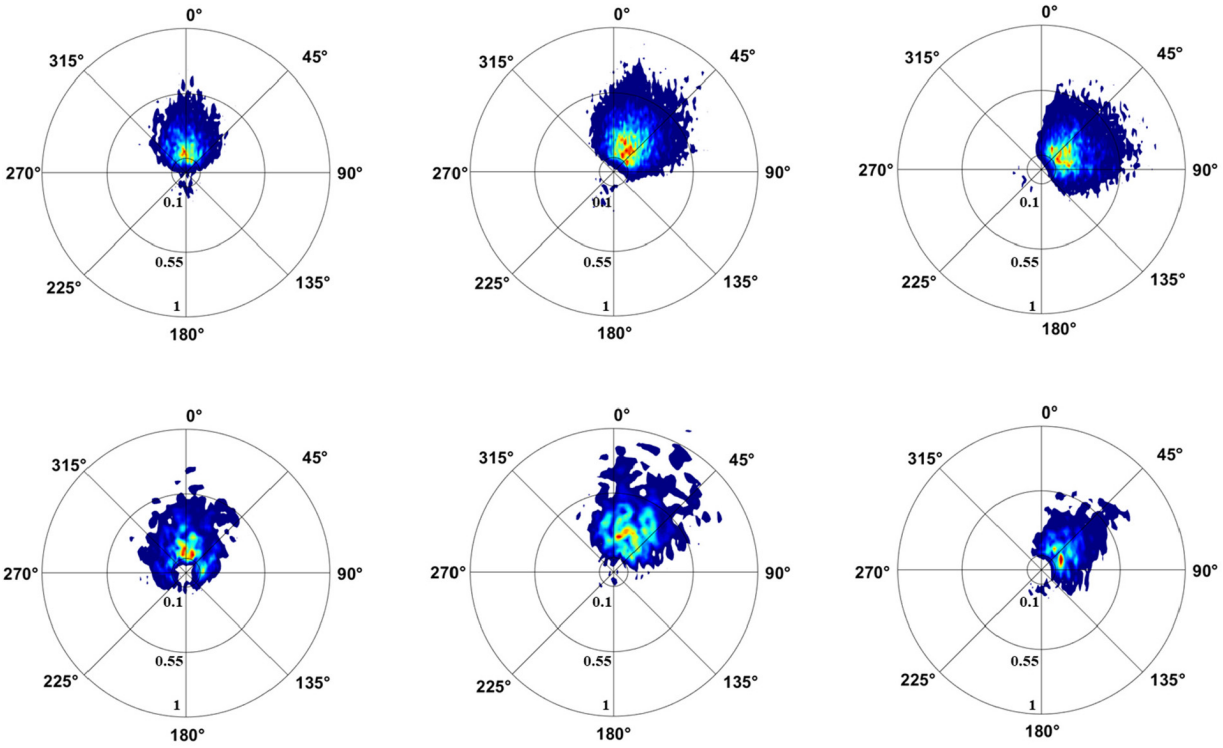

Fig. 9. 2-D directional spectra related to (left) WF_1, (middle) WF_2, and (right) WF_3. (Top) Retrieved directional spectra. (Bottom) True sea wave directional spectra. Radius corresponds to wavenumber k. Color scale [0, 1].

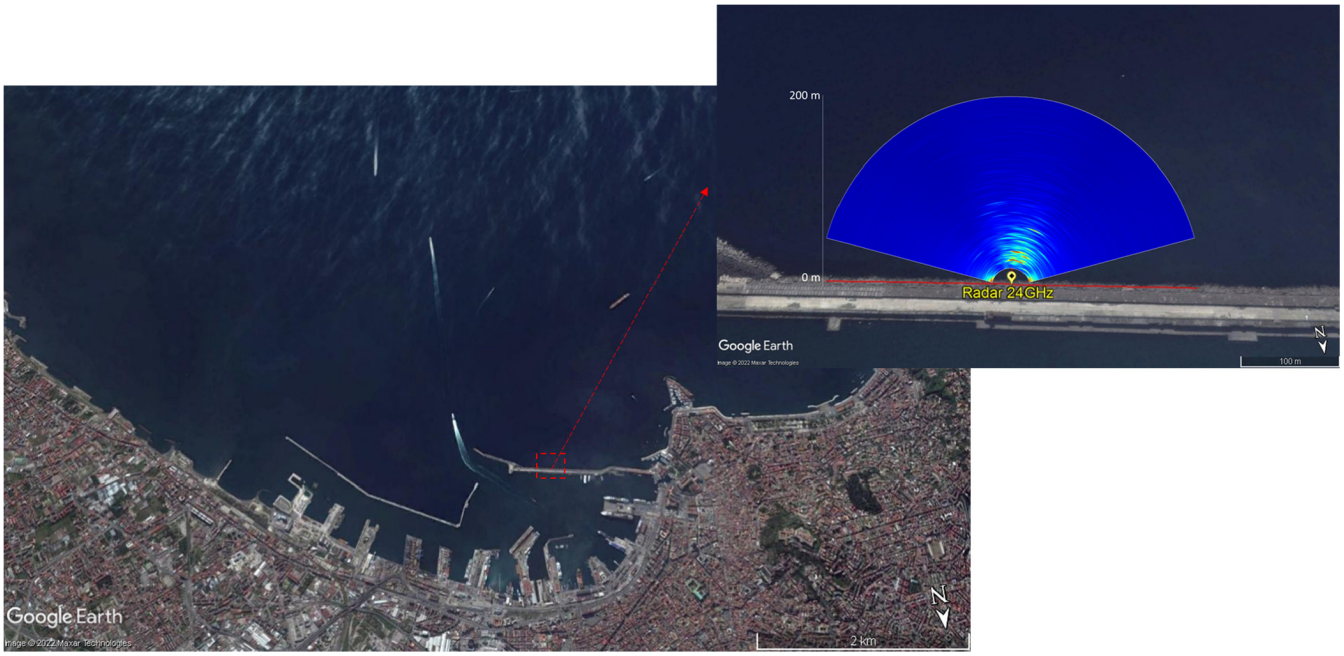

Fig. 10. Satellite photograph of the investigated area provided by Google Earth Pro. Inset: Radar location superimposed on a radar image.

λ_{peak}, direction θ_{peak}, and wind speed W_{10} (see Table II for details). The significant wave height and sea surface current components are set equal to $H_s = 1.2$ m, $U_x = 0.6$ m·s^{-1}, and $U_y = 0.3$ m·s^{-1}. The sea surface elevation profile in (6) is computed over a Cartesian grid with spacing $\Delta x = \Delta y = 1$ m.

A temporal sequence of $M = 256$ data frames is produced by the simulator described in Section III-B. The time interval between two consecutive frames is equal to $\Delta t = 0.5$ s, leading to a total observation time equal to $T_w = 128$ s. The electrical and geometrical parameters of the radar considered for the present numerical analysis are similar to those of the radar

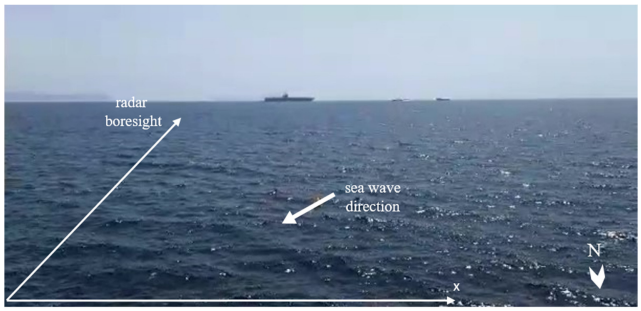

Fig. 11. Photograph of the investigated area taken during the data acquisition. The arrows denote the radar boresight and sea wave arrival direction.

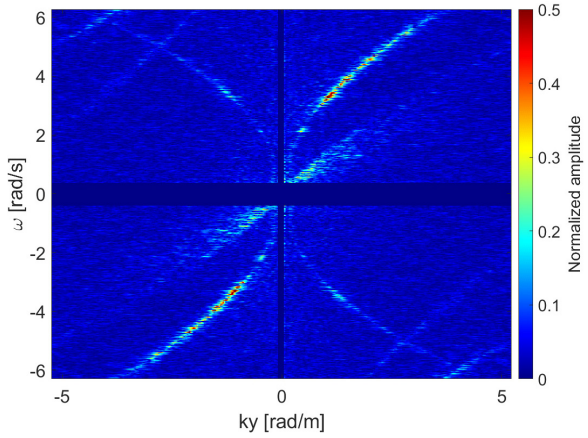

Fig. 12. Cut of 3-D radar data spectrum for radar data acquired during the experimental test.

prototype used for the experimental phase, as summarized in Table III. In particular, the radar antenna is located at a height $h = 10$ m above the MSL and it is tilted in the vertical plane as in Fig. 4 achieving a range coverage from $\rho_{\min} = 34$ m to $\rho_{\max} = 164$ m above the MSL.

The radar images are generated on a polar grid via beamforming in accordance with the aforementioned range coverage and azimuth FoV ($\pm 75°$). After that, they are interpolated over a uniform Cartesian grid by considering a spatial discretization step identical to the sea WF one.

An example of synthetic data related to WF_1 at time $\tilde{t} = 64$ s is shown in Fig. 6. The top panel is a snapshot of the sea wave elevation profile and the bottom panel is the corresponding radar image. Most notably, the radar data spectrum shown in Fig. 7 has the typical form of a dispersion relation, thus suggesting the possibility to exploit radar images for sea wave monitoring. Note that the image in Fig. 7 has been obtained by computing the 3-D radar spectrum from the sequence of $M = 256$ images and taking the cut in the plane $k_x = 0$.

At this point, the sea surface currents are estimated by processing the whole temporal sequence of radar images. To this end, the spatial partitioning technique in Fig. 5 is applied with a twofold aim. The first aim is the assessment of the estimation procedure described in Section IV for an SRK-band FMCW MIMO radar. The second aim is the determination of the reliability area, i.e., the region in the radar FoV where the surface current estimation can be considered reliable. Indeed, the energy of the radar spectrum decays far from the direction of the incoming sea wave. Moreover, as said above, the radar angular resolution degrades significantly toward the edges of the FoV, which implicitly makes the data less accurate.

The radar images are partitioned by considering N_s subareas with size 70 × 70 m and an overlap of 10 m along both x- and y-directions. Note that, as the WFs have been generated by considering a spatially uniform surface current on the entire area investigated by the radar, the retrieved currents in each subarea are expected to be similar in terms of intensity and direction. For each subarea, the estimation accuracy of the surface currents is quantified by the relative percentage error (RPE)

$$\mathrm{RPE} = \left\{ \frac{\left| \hat{\bar{U}}_j^{(\mathrm{estimate})} - \bar{U}_j^{(\mathrm{true})} \right|}{\left| \bar{U}_j^{(\mathrm{true})} \right|} \times 100 \right\}_{j=1,\ldots,N_s}. \tag{18}$$

Accordingly, based on (18), it is possible to produce an error map for surface currents, which allows visualization of the reconstruction accuracy within the radar FoV.

An additional figure of merit defined as reliability index (RI) is here introduced to assess the global reliability of the surface current estimate, i.e.,

$$\mathrm{RI} = \frac{N_{\mathrm{csce}}}{N_{\mathrm{sce}}} \times 100. \tag{19}$$

In (19), N_{csce} is the number of local estimates ensuring an RPE lower than a threshold value T_h and N_{sce} is the total number of estimates in the radar FoV. Note that a maximum percentage error $T_h = 5\%$ is here assumed since this value is considered tolerable according to literature data [33], [46], [47].

The reconstructed sea surface current maps for the three considered WFs are shown in Fig. 8(a), (c), and (e), where they are superimposed on the radar image at $\tilde{t} = 5$ s. Fig. 8(b), (d), and (f) shows the spatial behavior of the RPE for the three considered cases. As stated before, the RPE exhibits a spatially varying behavior and generally increases when the observation direction is far from the direction of the incoming sea WF. Moreover, if the sea WF direction differs significantly from the radar boresight [see Fig. 8(f)], the reconstructed map turns out to be reliable over a smaller angular sector. This phenomenon is quantified by the RI values, which are equal to 76%, 55%, and 48% for WF_1, WF_2, and WF_3, respectively. Finally, it is also observed that the minimum error is generally achieved in a small angular sector around the direction of arrival of the incoming sea WF.

Based on the estimated sea surface currents, a bandpass filter is built (see the flowchart in Fig. 5) to filter the 3-D radar spectrum referred to the entire observed area. After, the peak wave direction θ_{peak} is retrieved from the 2-D directional spectrum [see (17)]. In this regard, Fig. 9 shows the retrieved 2-D directional spectra for all considered WFs and the corresponding true sea wave directional spectra. The θ_{peak} values retrieved from such spectra are equal to 0°, 29°, and 58° for WF_1, WF_2, and WF_3, respectively. These values turn

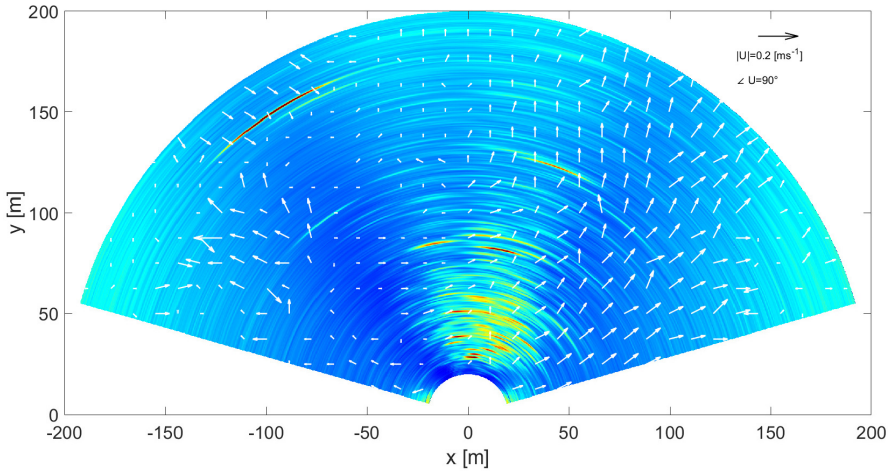

Fig. 13. Retrieved sea surface current map superimposed on the radar image at $\tilde{t} = 5$ s. Reference values are shown for the magnitude and direction of the surface currents. The direction of the dominant wave with respect to the radar boresight is $\theta_{\text{peak}} \approx 27°$.

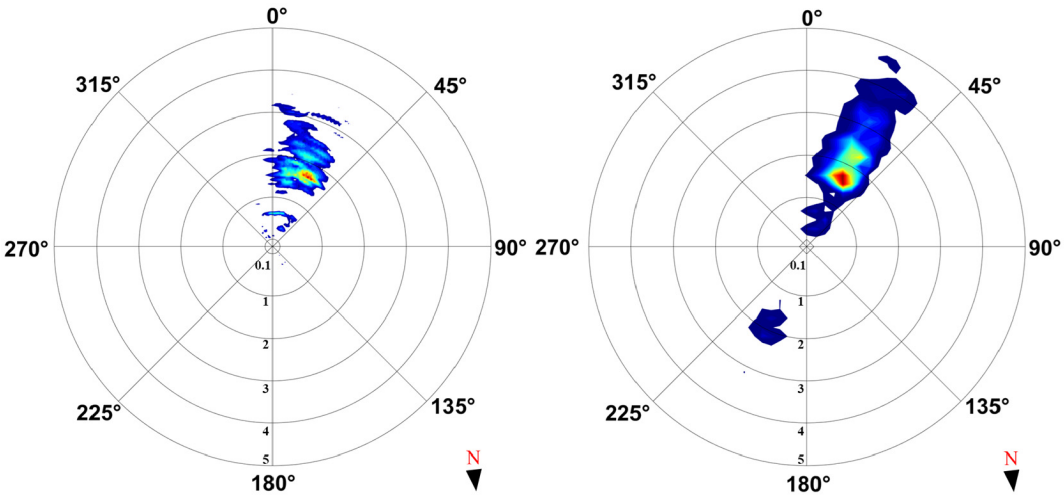

Fig. 14. (Left) Directional spectrum of entire area. (Right) Directional spectrum related to the subarea centered at $x = 44$ m and $y = 62.5$ m. The radius corresponds to wavenumber k.

out to be in close agreement with nominal sea WF directions listed in Table II.

VI. Experimental Test

This section aims at assessing the capabilities of the radar system and its data processing pipeline to estimate the sea surface current and directional wave spectra in a real marine environment. A field trial was carried out on May 10, 2022 (01:30 P.M. local time) at San Vincenzo quay in the port area of Naples, Italy. A satellite picture of the investigated area provided by Google Earth Pro is shown in Fig. 10, where the inset shows the radar location superimposed on a radar image.

The geographical coordinates of the radar (40°50′ 1.12″N, 14°16′ 4.61″E) and the direction of the antenna boresight to the north (170° SE) were evaluated by using the GNSS receiver and the magnetic compass of a smartphone, respectively. The radar was installed inside a waterproof case and mounted on a tripod at an approximate height of 10 m above the MSL. During the experimental test, the information about the wind speed was not recorded since no weather station was available close to the port area. However, based on an anemometric station located at Naples airport, about 5 km away from the measurement site, the average wind speed during the radar data acquisition was equal to 2.1 m/s. This value is lower than 3 m/s; however, since the experimental test was carried out on a quay at 1.5 km from the coast (i.e., off-shore), it is expected that wind speed was higher than the average value recorded in the city due to the local breeze. Accordingly, the local wind speed was sufficient to generate capillary waves on the sea surface so to induce significant backscattering. A photograph was taken during the data acquisition to appreciate in a qualitative way the sea conditions (see Fig. 11).

Specifically, the data were recorded on a sunny day with a light breeze (Beaufort scale [48]) from the SW direction that induces a slight sea (Douglas scale [45]). Moreover, the considered area is characterized by a seabed varying in the range of 10–26 m [49]. By accounting that most of radar image spectrum energy is concentrated at wavenumbers $k > 1$ rad/m

(see Fig. 12) and evaluating the hyperbolic tangent [see (9)] at the minimum depth (i.e., $D = 10$ m), it follows that the deep-sea water condition is valid to process the radar data. The radar configuration parameters are the same listed in Table III except for $\rho_{\min}$ and $\rho_{\max}$, which are equal to 20 and 200 m, respectively. Moreover, the radar image interpolation on the Cartesian grid was carried out by considering a uniform pixel spacing $\Delta x = \Delta y = 0.2$ m.

The sea surface current map shown in Fig. 13 is obtained by partitioning the radar images into N_s subareas with size 30×30 m and an overlap of 10 m along both x- and y-directions. Even though no ground truth for surface currents is available, due to the complex experimentation involved, the vector field in Fig. 13 exhibits a realistic and almost continuous trend in the right half of the image around the arrival direction of sea waves.

The retrieved surface currents are later exploited to filter the radar spectrum on the whole observed area. Based on the marine weather conditions, the magnitude of sea surface currents is expected to be on average close to 0.2 m/s. Therefore, in order to properly build the bandpass filter, the outliers with a magnitude greater than 0.3 m/s are removed.

The left panel in Fig. 14 shows the 2-D directional spectrum of the whole area, from which the estimated direction of the dominant wave with respect to the radar boresight is $\theta_{\text{peak}} \approx 27°$. Based on the analysis performed on the numerical data in Section V (see Fig. 8), it is expected that the region where the estimated sea surface currents can be considered reliable is around the direction of incoming sea waves. This conjecture turns out to be consistent with the sea surface current field formerly shown in Fig. 13, where a well-defined trend is observed nearby the arrival direction of the sea waves.

Finally, the directional spectrum is evaluated on a subarea located in correspondence with the direction of the incoming waves and close to the quay. Specifically, the subarea is centered at $x = 44$ m, $y = 62.5$ m, and here, the retrieved sea surface current components are equal to $\hat{U}_x = 0.12$ m·s^{-1} and $\hat{U}_y = 0.02$ m·s^{-1}. The achieved result is shown in the right panel of Fig. 14, where the brighter spot is related to the spectral density of the incident wave ($\theta_{\text{peak}} \approx 27°$), while the weaker spot in the third quadrant accounts for the reflected wave ($\theta_{\text{peak}} \approx 207°$). Both directions are measured clockwise with respect to the radar boresight. By evaluating the ratio between the peak energy of the incident and reflected waves, it turns out that the breakwater adjacent to the quay reduces the energy of the incoming dominant wave of about 70%. This value is consistent with previously published data [17], [50].

VII. Conclusion

A feasibility study regarding the possible exploitation of an automotive 24 GHz FMCW MIMO radar for land-based sea wave monitoring has been presented in this article.

A two-step data processing pipeline has been applied to estimate the sea surface currents maps and directional spectrum. The radar system capabilities have been first assessed on synthetic data. To this end, sea WFs with different characteristics have been generated by the Fourier domain approach. Then, the radar returns from the sea surface have been computed by resorting to a simplified scattering model accounting for the tilt and shadowing modulation effects. As shown, the minimum error on the retrieved surface currents is achieved in a small angular region around the direction of the incoming sea waves.

An experimental test carried out in a port area has confirmed that the reconstruction of the surface currents has a reliable behavior in an angular sector around the arrival direction of the sea waves. Moreover, the analysis of the directional spectrum has allowed identifying the direction of the incoming sea wave and that of the wave reflected by the quay.

Despite the achieved results being preliminary, they suggest that SRK-band FMCW MIMO radar can be a valid remote sensing tool for sea wave monitoring. However, such a system suffers from a limited angular resolution far from the boresight direction, which leads to some inaccuracies in surface currents' estimation. This limitation could be overcome by considering the mechanical rotation of the radar system or deploying multiple radar units.

In future work, a long-term analysis regarding the combined use of this radar and another wave sensor (e.g., buoy) may be performed to evaluate an MTF in order to calibrate the radar image spectrum. This would allow a reliable estimation of sea state parameters (e.g., significant wave height, period, and wavelength) as well as the reconstruction of the sea WF. Furthermore, the performance of the radar system will be analyzed also in not-fully developed sea conditions. A further analysis could involve the simulation of more complex wave spectra considering different types of spreading as well as the propagation of the sea wave in intermediate and shallow water conditions.

Acknowledgment

The authors would like to thank Dr. Antonio Natale for the useful discussion on electromagnetic scattering models from the sea surface and Dr. Matteo Postacchini and Dr. Claudio Lugni for discussions on sea wave propagation models.

References

[1] E. D. R. Shearman, "Radio science and oceanography," *Radio Sci.*, vol. 18, no. 3, pp. 299–320, May 1983, doi: 10.1029/RS018i003p00299.

[2] D. B. Chelton, J. C. Ries, B. J. Haines, L. Fu, and P. S. Callahan, "Satellite altimetry," in *Satellite Altimetry and Earth Sciences: A Handbook of Techniques and Applications*, 1st ed., L.-L. Fu and A. Cazenave, Eds. San Diego, CA, USA: Academic, 2001, pp. 1–131.

[3] A. Benetazzo et al., "Stereo imaging and X-band radar wave data fusion: An assessment," *Ocean Eng.*, vol. 152, pp. 346–352, Mar. 2018.

[4] M. Streser, R. Carrasco, and J. Horstmann, "Video-based estimation of surface currents using a low-cost quadcopter," *IEEE Geosci. Remote Sens. Lett.*, vol. 14, no. 11, pp. 2027–2031, Nov. 2017.

[5] S. P. Neill and M. R. Hashemi, "In situ and remote methods for resource characterization," in *E-Business Solutions, Fundamentals of Ocean Renewable Energy*, S. P. Neill and M. R. Hashemi. New York, NY, USA: Academic, 2018, pp. 157–191.

[6] G. Ludeno and M. Uttieri, "Editorial for special issue 'radar technology for coastal areas and open sea monitoring,"' *J. Mar. Sci. Eng.*, vol. 8, no. 8, p. 560, Jul. 2020.

[7] R. M. Goldstein, H. A. Zebker, and T. P. Barnett, "Remote sensing of ocean currents," *Science*, vol. 246, no. 4935, pp. 1282–1285, Aug. 1989.

[8] F. Ardhuin et al., "Measuring currents, ice drift, and waves from space: The sea surface kinematics multiscale monitoring (SKIM) concept," *Ocean Sci. Discus.*, vol. 2017, pp. 1–26, May 2017.

[9] A. Natale, G. Jackson, C. Esposito, G. Fornaro, R. Lanari, and S. Perna, "Sea state observation through a three-antenna hybrid XT/AT InSAR configuration: A preliminary study based on the $InSAeS_4$ airborne system," *Remote Sens.*, vol. 9, no. 8, p. 792, Aug. 2017.

[10] C. Mantovani et al., "Best practices on high frequency radar deployment and operation for ocean current measurement," *Frontiers Mar. Sci.*, vol. 7, p. 210, Apr. 2020.

[11] H. Roarty et al., "The global high frequency radar network," *Frontiers Mar. Sci.* vol. 6, p. 164, Dec. 2019.

[12] J. P.-Y. Maa and H. K. Ha, *X-Band Radar Wave Observation System Field Testing of a Physical/Biological Monitoring Methodology for Offshore Dredging and Mining Operations*, vol. 56. Washington, DC, USA: U.S. Department of the Interior, Minerals Management Service, 2005.

[13] H.-Y. Cheng and H. Chien, "Implementation of S-band marine radar for surface wave measurement under precipitation," *Remote Sens. Environ.*, vol. 188, pp. 85–94, Jan. 2017.

[14] I. R. Young, W. Rosenthal, and F. Ziemer, "A three-dimensional analysis of marine radar images for the determination of ocean wave directionality and surface currents," *J. Geophys. Res.*, vol. 90, no. C1, pp. 1049–1059, 1985.

[15] R. Gangeskar, "An algorithm for estimation of wave height from shadowing in X-band radar sea surface images," *IEEE Trans. Geosci. Remote Sens.*, vol. 52, no. 6, pp. 3373–3381, Jul. 2013.

[16] G. Ludeno and F. Serafino, "Estimation of the significant wave height from marine radar images without external reference," *J. Mar. Sci. Eng.*, vol. 7, no. 12, p. 432, 2019.

[17] G. Ludeno et al., "Remocean system for the detection of the reflected waves from the Costa concordia ship wreck," *IEEE J. Sel. Topics Appl. Earth Observ. Remote Sens.*, vol. 7, no. 7, pp. 3011–3018, Jul. 2014.

[18] C. M. Senet, J. Seemann, S. Flampouris, and F. Ziemer, "Determination of bathymetric and current maps by the method DiSC based on the analysis of nautical X-band radar image sequences of the sea surface (November 2007)," *IEEE Trans. Geosci. Remote Sens.*, vol. 46, no. 8, pp. 2267–2279, Aug. 2008.

[19] G. Ludeno et al., "Normalized scalar product approach for nearshore bathymetric estimation from X-band radar images: An assessment based on simulated and measured data," *IEEE J. Ocean. Eng.*, vol. 43, no. 1, pp. 221–237, Oct. 2017.

[20] B. Lund, H. C. Graber, K. Hessner, and N. J. Williams, "On shipboard marine X-band radar near-surface current 'calibration,'" *J. Atmos. Ocean. Technol.*, vol. 32, no. 10, pp. 1928–1944, Oct. 2015.

[21] G. Ludeno, A. Orlandi, C. Lugini, C. Brandini, F. Soldovieri, and F. Serafino, "X-band marine radar system for high-speed navigation purposes: A test case on a cruise ship," *IEEE Geosci. Remote Sens. Lett.*, vol. 11, no. 1, pp. 244–248, Jan. 2014.

[22] J. C. Nieto-Borge, G. R. Rodríguez, K. Hessner, and P. I. González, "Inversion of marine radar images for surface wave analysis," *J. Atmos. Ocean. Technol.*, vol. 21, pp. 1291–1300, Aug. 2004.

[23] W. Navarro, J. C. Velez, A. Orfila, and S. Lonin, "A shadowing mitigation approach for sea state parameters estimation using X-band remotely sensing radar data in coastal areas," *IEEE Trans. Geosci. Remote Sens.*, vol. 57, no. 9, pp. 6292–6310, Sep. 2019.

[24] R. Carrasco, J. Horstmann, and J. Seemann, "Significant wave height measured by coherent X-band radar," *IEEE Trans. Geosci. Remote Sens.*, vol. 55, no. 9, pp. 5355–5365, Sep. 2017.

[25] Z. Chen, C. Zhang, C. Zhao, X. Chen, and H. Liu, "Peak wave direction measurement using shipboard coherent microwave radar," *IEEE Geosci. Remote Sens. Lett.*, vol. 19, no. 9, pp. 1–5, Aug. 2021.

[26] J. Cui, R. Bachmayer, W. Huang, and B. deYoung, "Wave height measurement using a short-range FMCW radar for unmanned surface craft," in *Proc. OCEANS MTS/IEEE Washington*, Oct. 2015, pp. 1–5, doi: 10.23919/OCEANS.2015.7404392.

[27] J. Cui, R. Bachmayer, B. deYoung, and W. Huang, "Ocean wave measurement using short-range K-band narrow beam continuous wave radar," *Remote Sens.*, vol. 10, no. 8, p. 1242, Aug. 2018.

[28] J. Cui, R. Bachmayer, B. de Young, and W. Huang, "Experimental investigation of ocean wave measurement using short-range K-band radar: Dock-based and boat-based wind wave measurements," *Remote Sens.*, vol. 11, no. 13, p. 1607, Jul. 2019.

[29] A. Stateczny, W. Kazimierski, D. Gronska-Sledz, and W. Motyl, "The empirical application of automotive 3D radar sensor for target detection for an autonomous surface Vehicle's navigation," *Remote Sens.*, vol. 11, no. 10, p. 1156, May 2019.

[30] G. Gennarelli, C. Noviello, G. Ludeno, G. Esposito, F. Soldovieri, and I. Catapano, "24 GHz FMCW MIMO radar for marine target localization: A feasibility study," *IEEE Access*, vol. 10, pp. 68240–68256, 2022.

[31] *INRAS*. Accessed: Jan. 18, 2023. [Online]. Available: http://www.inras.at/en/products/radarbook.html

[32] C. M. Schmid, R. Feger, C. Pfeffer, and A. Stelzer, "Motion compensation and efficient array design for TDMA FMCW MIMO radar systems," in *Proc. 6th Eur. Conf. Antennas Propag. (EUCAP)*, Mar. 2012, pp. 1746–1750.

[33] G. Ludeno, C. Nasello, F. Raffa, G. Ciraolo, F. Soldovieri, and F. Serafino, "A comparison between drifter and X-band wave radar for sea surface current estimation," *Remote Sens.*, vol. 8, no. 9, p. 695, Aug. 2016.

[34] M. Postacchini and G. Ludeno, "Combining numerical simulations and normalized scalar product strategy: A new tool for predicting beach inundation," *J. Mar. Sci. Eng.*, vol. 7, no. 9, p. 325, Sep. 2019.

[35] G. Mastin, P. Watterberg, and J. Mareda, "Fourier synthesis of ocean scenes," *IEEE Comput. Graph. Appl.*, vol. VCG-7, no. 3, pp. 16–23, Mar. 1987, doi: 10.1109/MCG.1987.276961.

[36] J. Tessendorf, "Simulating ocean water," *SIGGRAPH*, vol. 1, no. 2, p. 5, 2001.

[37] W. J. Pierson and L. Moskowitz, "A proposed spectral from for fully developed windforms based on the similarity theory of S. A. Kitaigorodskii," *J. Geophys. Res.*, vol. 69, no. 24, pp. 5181–5190, 1964.

[38] L. H. Holthuijsen, *Waves in Oceanic and Coastal Waters*. Cambridge, U.K.: Cambridge Univ. Press, 2010.

[39] M. Zhang, H. Chen, and H.-C. Yin, "Facet-based investigation on EM scattering from electrically large sea surface with two-scale profiles: Theoretical model," *IEEE Trans. Geosci. Remote Sens.*, vol. 49, no. 6, pp. 1967–1975, Jun. 2011.

[40] A. Iodice, A. Natale, and D. Riccio, "Retrieval of soil surface parameters via a polarimetric two-scale model," *IEEE Trans. Geosci. Remote Sens.*, vol. 49, no. 7, pp. 2531–2547, Jul. 2011.

[41] A. Iodice, A. Natale, and D. Riccio, "Kirchhoff scattering from fractal and classical rough surfaces: Physical interpretation," *IEEE Trans. Antennas Propag.*, vol. 61, no. 4, pp. 2156–2163, Apr. 2013.

[42] O. M. Phillips, "Radar returns from the sea surface—Bragg scattering and breaking waves," *J. Phys. Oceanogr.*, vol. 18, no. 8, pp. 1065–1074, Aug. 1988.

[43] H. Chen, M. Zhang, Y.-W. Zhao, and W. Luo, "An efficient slope-deterministic facet model for SAR imagery simulation of marine scene," *IEEE Trans. Antennas Propag.*, vol. 58, no. 11, pp. 3751–3756, Nov. 2010.

[44] S. Salcedo-Sanz, J. C. Nieto Borge, L. Carro-Calvo, L. Cuadra, K. Hessner, and E. Alexandre, "Significant wave height estimation using SVR algorithms and shadowing information from simulated and real measured X-band radar images of the sea surface," *Ocean Eng.*, vol. 101, pp. 244–253, Apr. 2015.

[45] E. H. Owens, "Sea conditions," in *Beaches and Coastal Geology*. (Encyclopedia of Earth Sciences Series). New York, NY, USA: Springer, 1982.

[46] W. Huang, R. Carrasco, C. Shen, E. W. Gill, and J. Horstmann, "Surface current measurements using X-band marine radar with vertical polarization," *IEEE Trans. Geosci. Remote Sens.*, vol. 54, no. 5, pp. 2988–2997, May 2016.

[47] B. Lund et al., "Near-surface current mapping by shipboard marine X-band radar: A validation," *J. Atmos. Ocean. Technol.*, vol. 35, no. 5, pp. 1077–1090, May 2018.

[48] E. H. Owens, "Beaufort wind scale," in *Beaches and Coastal Geology* (Encyclopedia of Earth Sciences Series). New York, NY, USA: Springer, 1982.

[49] *Terra Map*. Accessed: Jan. 18, 2023. [Online]. Available: https://www.globalterramaps.com/MBViewer.html?layer=2&pres=2&udw=2&nostore=1&lat=37.13&lng=-97.33&zoom=4

[50] G. Ludeno et al., "An X-band radar system for bathymetry and wave field analysis in a Harbour area," *Sensors*, vol. 15, pp. 1691–1707, Jan. 2015.

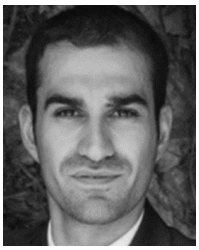

Giovanni Ludeno received the M.S. degree in telecommunication engineering from the University "Mediterranea" of Reggio Calabria, Reggio Calabria, Italy, in 2011, and the Ph.D. degree in electronics and computer engineering from the University of Campania "Luigi Vanvitelli," Caserta, Italy, in 2015.

From November 2011 to October 2012, he was a Scholar with the Institute for Electromagnetic Sensing of the Environment, National Research Council of Italy (IREA-CNR), Naples, Italy. From October 2012 to January 2014, he was a Research Fellow with Vitrociset SpA, Rome, Italy. Since 2015, he has been a Research Scientist with IREA-CNR. He has coauthored over 60 publications in international peer-reviewed journals, conference proceedings, and books. His research interests include the field of applied electromagnetism, with special regard to remote and in situ sensing.

Dr. Ludeno was a Guest Editor for a Special Issue of the *Journal of Marine Science of Engineering* (MDPI), where he is currently a Topic Editor.

Ilaria Catapano received the Ph.D. degree in electric and information engineering from the University of Cassino, Cassino, Italy, in 2006.

In 2003, in the framework of her Ph.D. project, she started her research activity with the Institute for Electromagnetic Sensing of the Environment, National Research Council of Italy (IREA-CNR), Naples, Italy, where she is currently a Full-Time Researcher. She was a Post-Doctoral Researcher with the Institute Fresnel of Marseille, Marseille, France, from October 2006 to March 2007. She joined the Mediterranea University of Reggio Calabria, Reggio Calabria, Italy, as an Adjunct Professor of electromagnetic diagnostic, in 2010; Sao Paulo University, Sao Paulo, Brazil, as an Invited Lecturer, in 2013; and IIT Kharagpur, Kharagpur, India, in 2016. She has coauthored more than 150 articles, mainly on scientific journals or proceedings of international conferences, and a reviewer for several international journals and conferences. Her research interests include noninvasive electromagnetic diagnostics and are mainly focused on models and strategies for electromagnetic forward and inverse scattering problems, development and performance assessment of microwave imaging approaches for shape reconstruction, and the processing of experimental data gathered by radar systems for subsurface surveys and terahertz (THz) spectroscopy and imaging.

Dr. Catapano received the G. Barzilai Award from the Italian Electromagnetic Society in 2004; she was one of the young scientist awardees at the XXIX URSI General Assembly in 2008.

Francesco Soldovieri (Senior Member, IEEE) is currently a Research Director of the Institute for Electromagnetic Sensing of the Environment, CNR, Naples, Italy. He has coauthored about 240 articles on national and international journals and more than 350 conference proceedings. His research interests include radar imaging, data processing for ground penetrating radar (GPR), indoor surveillance, through-wall imaging, passive radars, integration of geophysical data, and radars for planetary exploration.

Mr. Soldovieri was the General Chair of the International Workshop on Advanced GPR 2007 and the General Co-Chair of the GPR Conference 2010. He was a member of the Editorial Board of IEEE-Geoscience and Remote Sensing Letters (GRSL). He is currently a member of the IEEE-Transactions on Computational Imaging (TCI), IEEE TRANSACTIONS ON GEOSCIENCE AND REMOTE SENSING (TGRS), and *Remote Sensing* (MDPI). He is an Editor-in-Chief of HERITAGE, an MDPI journal devoted to *Cultural and Natural Heritage*. He has been the Scientific Coordinator of the FP7 projects ISTIMES and AMISS and the Technical Manager of the H2020 Project HERACLES. He was the President of the Division on Geosciences Instrumentation and Data Systems of European Geosciences Union.

Gianluca Gennarelli received the M.Sc. degree (summa cum laude) in electronic engineering and the Ph.D. degree in information engineering from the University of Salerno, Salerno, Italy, in 2006 and 2010, respectively.

From 2010 to 2011, he was a Post-Doctoral Fellow with the University of Salerno. In 2015, he joined the NATO-CMRE, La Spezia, Italy, as a Visiting Scientist. Since 2012, he has been a Research Scientist with the Institute for Electromagnetic Sensing of the Environment, National Research Council of Italy (IREA-CNR), Naples, Italy. He has coauthored over 100 publications in international peer-reviewed journals and conference proceedings. He serves as a reviewer for several international journals and conference papers. His research interests include microwave sensors, antennas, inverse scattering problems, radar imaging and signal processing, diffraction problems, and electromagnetic simulation.

Open Access funding provided by 'Consiglio Nazionale delle Ricerche-CARI-CARE' within the CRUI CARE Agreement